MOLECULAR AND CELLULAR BIOLOGY, Sept. 2005, p. 8299–8310 Vol. 25, No. 18
0270-7306/05/$08.00+0 doi:10.1128/MCB.25.18.8299–8310.2005

Targeted Ablation of the *Abcc6* Gene Results in Ectopic Mineralization of Connective Tissues

John F. Klement,[1]†* Yasushi Matsuzaki,[1]† Qiu-Jie Jiang,[1] Joseph Terlizzi,[1] Hae Young Choi,[1] Norihiro Fujimoto,[1] Kehua Li,[1] Leena Pulkkinen,[1] David E. Birk,[2] John P. Sundberg,[4] and Jouni Uitto[1,3]

Departments of Dermatology and Cutaneous Biology,[1] Pathology, Anatomy, and Cell Biology,[2] and Biochemistry and Molecular Pharmacology,[3] Jefferson Medical College, Jefferson Institute of Molecular Medicine, Thomas Jefferson University, Philadelphia, Pennsylvania, and The Jackson Laboratory, Bar Harbor, Maine[4]

Received 30 March 2005/Returned for modification 1 June 2005/Accepted 17 June 2005

Pseudoxanthoma elasticum (PXE), characterized by connective tissue mineralization of the skin, eyes, and cardiovascular system, is caused by mutations in the *ABCC6* gene. *ABCC6* encodes multidrug resistance-associated protein 6 (MRP6), which is expressed primarily in the liver and kidneys. Mechanisms producing ectopic mineralization as a result of these mutations remain unclear. To elucidate this complex disease, a transgenic mouse was generated by targeted ablation of the mouse *Abcc6* gene. *Abcc6* null mice were negative for Mrp6 expression in the liver, and complete necropsies revealed profound mineralization of several tissues, including skin, arterial blood vessels, and retina, while heterozygous animals were indistinguishable from the wild-type mice. Particularly striking was the mineralization of vibrissae, as confirmed by von Kossa and alizarin red stains. Electron microscopy revealed mineralization affecting both elastic structures and collagen fibers. Mineralization of vibrissae was noted as early as 5 weeks of age and was progressive with age in *Abcc6*$^{-/-}$ mice but was not observed in *Abcc6*$^{+/-}$ or *Abcc6*$^{+/+}$ mice up to 2 years of age. A total body computerized tomography scan of *Abcc6*$^{-/-}$ mice revealed mineralization in skin and subcutaneous tissue as well as in the kidneys. These data demonstrate aberrant mineralization of soft tissues in PXE-affected organs, and, consequently, these mice recapitulate features of this complex disease.

The human *ABCC6* gene encodes MRP6, a member of the family of multidrug resistance-associated proteins (MRPs) belonging to the ATP-binding cassette (ABC) superfamily of membrane transporters (9, 27). The MRP6 protein was predicted to consist of three membrane-spanning domains comprised of 5, 6, and 6 transmembrane segments, respectively (5, 6). The intracellular portion of the protein displays two nucleotide binding folds, both having conserved Walker A and B ATP-binding motifs critical for the function of this class of proteins as transmembrane transporters. The precise function of MRP6 is currently unknown, but it has ~45% homology to MRP1, the prototype within subfamily C of ABC proteins. MRP1 is instrumental to cellular detoxification and has the capacity to confer chemotherapy resistance to cells (9, 27). The expression of the *ABCC6* gene was demonstrated primarily, if not exclusively, at the basolateral surface of hepatocytes and kidney tubules (4, 6). Thus, based on structural homology with MRP1 and its selective tissue location, it was suggested that MRP6 serves as an efflux pump eliminating metabolic compounds from the intracellular milieu (62). It was shown in vitro that glutathione S-conjugates are transported by MRP6 and that MRP6 confers low-level resistance to several anticancer drugs; however, its natural substrates in vivo remain undefined (5, 24).

* Corresponding author. Mailing address: Department of Dermatology and Cutaneous Biology, Jefferson Medical College, 233 S. 10th Street, Suite 322 BLSB, Philadelphia, PA 19107. Phone: (215) 503-4488. Fax: (215) 503-5788. E-mail: John.Klement@jefferson.edu.

† J.F.K. and Y.M. contributed equally to this study.

Interest in the *ABCC6*-MRP6 gene-protein system was heightened by recent demonstrations of mutations in this gene in pseudoxanthoma elasticum (PXE; Online Mendelian Inheritance in Man [OMIM] 264800 and 177850) (17, 29, 41, 42), an autosomal recessive multisystem disorder with cutaneous, ophthalmologic, and cardiovascular manifestations (32). A spectrum of mutations in the *ABCC6* gene was defined, with the characteristic inactivating mutations being nonsense mutations, out-of-frame insertions or deletions, or missense mutations affecting critical amino acids within the nucleotide binding fold domains (10, 38, 42).

The early clinical findings of PXE, often noticeable around puberty, consist of yellowish cutaneous papules encountered in primary predilection sites, such as the antecubital fossae and the sides of the neck. The primary lesions tend to coalesce into larger plaques rendering skin redundant and inelastic. Sagging of the skin often progresses with advancing age and may lead to a prematurely aged appearance of the affected individuals (32). Histopathologic examination of the cutaneous lesions reveals accumulation of pleomorphic elastotic material, demonstrating progressive mineralization. In addition, electron microscopy of the affected skin in patients with PXE shows mineralization of dermal collagen fibers (32). Involvement of skin, although primarily of cosmetic concern, signifies the association of pathological changes in the eyes and the cardiovascular system with considerable morbidity and mortality.

A characteristic ocular finding is the presence of angioid streaks, which result from breaks in the mineralized elastic lamina, the so-called Bruch's membrane (lamina basalis cho-

roideae), which is derived from the basement membranes of the retinal pigment epithelium and the choriocapillary endothelium. The fractures in this membrane result in neovascularization from the choriocapillaries, and the newly formed fragile blood vessels may break, leading to hemorrhage and scarring. These pathological changes can ultimately lead to progressive loss of visual acuity and, rarely, to legal blindness.

The third clinical component of PXE is the involvement of the cardiovascular system, particularly the mid-sized arterial blood vessels that become progressively mineralized. This process can lead to internal bleeding, particularly from the gastric vessels. Mineralization of the arteries in the legs can be accompanied by intermittent claudication, and calcification of the coronary arteries may lead to myocardial infarcts at a relatively early age of the affected individual. Thus, the diagnostic tissue lesions in PXE appear to consist of the mineralization of connective tissue in the skin, eyes, and the arterial blood vessels.

The incidence of PXE has been estimated to be around 1:100,000 (32), although the exact figure is unknown. In addition, it was recently suggested that a recurrent mutation in the *ABCC6* gene, R1141X, which is frequently encountered in Caucasian populations, is associated with a significantly increased risk for cardiovascular disease (59). The diagnosis of PXE is often difficult due to extensive inter- and intrafamilial variability and delayed onset of manifestations, frequently not evident until the second or third decade of life. Compounding the difficulty of establishing the correct diagnosis is the fact that some clinical conditions, such as actinic elastosis and cutis rhomboidalis nuchae, may mimic the cutaneous findings, while angioid streaks are not specific to PXE (61). At the same time, the mechanisms that lead to calcification of connective tissues in the skin, eyes, and the cardiovascular system as a result of mutations in the *ABCC6* gene, which is expressed primarily in the liver and the kidneys, are unclear. Finally, there is no treatment for this occasionally devastating condition. It is clear, therefore, that development of an animal model would potentially provide insight into this complex clinical condition. Toward development of an animal model for PXE, we generated a targeted mutant mouse in which both alleles of the mouse *Abcc6* gene have been inactivated by targeted ablation. Histopathologic, immunohistochemical, ultrastructural, and computerized tomography imaging analyses of these mice revealed extensive mineralization of a variety of connective tissues.

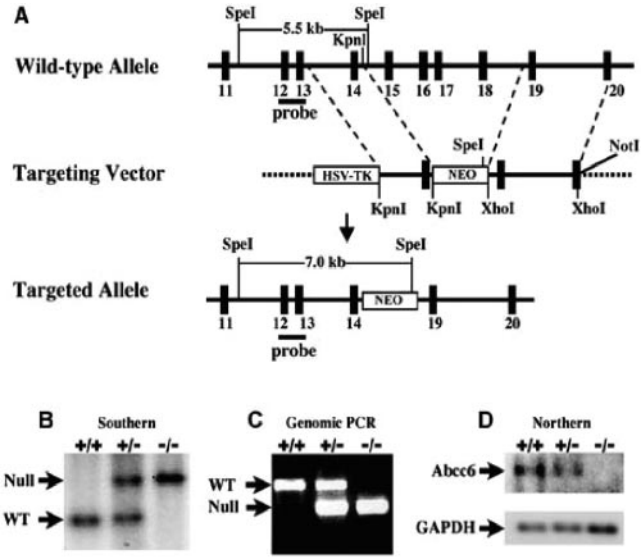

FIG. 1. Gene targeting of the mouse *Abcc6* locus. (A) Schematic diagram of the mouse *Abcc6* gene (exons 11 to 20) and the targeting vector containing HSV-TK and neomycin resistance (NEO) genes. Homologous recombination results in replacement of 7.1 kb of the mouse *Abcc6* gene, spanning from intron 14 to intron 18, by the neomycin resistance gene. Disruption of the *Abcc6* allele by introduction of the neomycin resistance gene alters the reading frame, resulting in accelerated mRNA decay. The vertical boxes represent *Abcc6* exons, and the horizontal lines represent introns, drawn to approximate scale. Note the presence of two SpeI restriction enzyme recognition sites in intron 11 and intron 14 of the wild-type allele. The downstream SpeI site is removed by gene targeting, while the neomycin resistance gene introduces a new SpeI site. Consequently, digestion of the wild-type and targeted alleles with SpeI results in 5.5-kb and 7.0-kb fragments, respectively, that can be recognized by a probe corresponding to exons 12 and 13. In the targeting vector diagram, the dashed lines denote plasmid vector sequences and the unique NotI site is indicated. (B) Southern blot analysis of DNA isolated from mouse tails allows genotyping of the mice upon digestion with SpeI. (C) Oligonucleotide primers (see Materials and Methods) allow PCR amplification of genomic DNA, resulting in synthesis of a 430-bp fragment from the wild-type allele and a 320-bp fragment from the targeted allele. (D) Northern blot analysis reveals a ~5-kb mRNA in total RNA isolated from the liver of wild-type (+/+) and heterozygous (+/−) mice, while no corresponding transcript is observed in −/− animals. Hybridization with a probe for GAPDH (glyceraldehyde-3-phosphate dehydrogenase) confirms the presence of RNA in all lanes in approximately equal quantities. WT, wild type.

MATERIALS AND METHODS

***Abcc6* gene targeting.** The mouse *Abcc6* DNA fragments utilized in construction of the gene-targeting vector and the probe for Southern DNA blot analysis are depicted in Fig. 1A and were generated using PCR. The oligonucleotides used for PCR amplification of 129Sv mouse genomic DNA are the following: 13Kpn-F, 5′-ATCCTGGtACCTGCTGGAAAGG-3′; 14-EcoRI-R, 5′-GTACCg aaTTCTGAGCACCTAGG-3′; 19Xho-F, 5′-ttcctttCCCTCgAGCGTGCGTAA CTTCTGC-3′; 20Xho-R, 5′-ttcccttcctcgagCTCCCACCTCCAGGAAAGC-3′; 12Kpn-F, 5′-ATTCCAGGCTGGTaCCTCTCTTGCC-3′; and 13-R, 5′-AGCTT TCTGACTCCTTGACC-3′. The nucleotides shown in lowercase do not match the *Abcc6* sequence but were incorporated to generate convenient restriction enzyme sites for plasmid construction. DNA cloning utilized standard methods (43, 44). The 3-kb 3′ *Abcc6* fragment was generated using oligonucleotides 19Xho-F and 20Xho-R, 129Sv mouse genomic DNA, and standard PCR conditions. The resulting DNA fragment was digested with XhoI (5′-CTCGAG-3′) as both oligonucleotides introduced XhoI restriction enzyme sites; it was ligated into the XhoI site (phosphatase treated) of pPNT (60) and used to transform competent *Escherichia coli* DH5α cells. The resulting plasmids were screened for the proper insert orientation, resulting in the generation of pPNT-3′*Abcc6*. The 2.2-kb 5′ *Abcc6* gene fragment was generated in a similar manner as the 3′ fragment using oligonucleotides 13Kpn-F and 14EcoRI-R and was then digested with KpnI (5′-GGTACC-3′). Oligonucleotide 13KpnF introduced one KpnI site, and the second KpnI site is an endogenous site located 3′ to exon 14 (Fig. 1A). The resulting DNA fragment was ligated into the KpnI site (phosphatase-treated) of pPNT-3′*Abcc6* used to transform *E. coli* DH5α, and the resulting plasmids were screened for proper DNA insert orientation. The complete *Abcc6* gene-targeting vector (pAbcc6-KO) is shown in Fig. 1A (Targeting Vector) and has the neomycin/G418 resistance (NEO) gene in the opposite transcriptional orientation relative to *Abcc6* genomic fragments, a herpes simplex virus-thymidine kinase (HSV-TK) gene, and a unique NotI restriction enzyme site to linearize the vector. Upon homologous recombination with endogenous *Abcc6*, a 7.1-kb DNA fragment encompassing exons 15 to 18 was replaced by the neomycin/G418 resistance gene (Fig. 1A). Southern DNA blot (44, 53) analysis was performed to distinguish the *Abcc6* wild-type and null alleles using a flanking 600-bp DNA probe produced by PCR amplification using oligonucleotides

12Kpn-F and 13R as above and encompassing *Abcc6* exons 12 and 13 (Fig. 1A). This DNA probe hybridizes with the ~5.5-kb SpeI restriction endonuclease-generated DNA fragment indicative of the wild-type allele and a ~7.0-kb DNA fragment indicative of the null allele (Fig. 1A and B).

Culture of mouse 129Sv embryonic stem (ES) cells (W9.5) (28), electroporation, selection, isolation of *Abcc6*$^{+/-}$ ES cells, blastocyst microinjection, and transfer of microinjected blastocysts to MF1 (Charles River Laboratories, Inc., Wilmington, MA) pseudopregnant mice were performed using standard procedures (1, 54). From approximately 500 ES cell clones, 5 *Abcc6*$^{+/-}$ clones were identified and 3 of these clones were used for microinjections into C57BL/6J (The Jackson Laboratory, Bar Harbor, ME) host blastocysts. Resulting chimeric male founder (F_0) mice were mated with C57BL/6J females and the agouti offspring (F_1) were genotyped by Southern DNA blot analysis as above. *Abcc6*$^{+/-}$ mice were mated to produce the *Abcc6* null mice (F_2 and F_3), which were fertile and were thus used to propagate the *Abcc6* null mouse line. The *Abcc6* mouse line was registered with the Institute for Laboratory Animal Research and is designated B6;129S1/SvImJ *Abcc6*^{tm1Jfk}. For the experiments described in this paper, the F_2 and F_3 generations were used, and the genotype designations have been shortened to *Abcc6*$^{-/-}$ for the null, *Abcc6*$^{+/-}$ for the heterozygous, and *Abcc6*$^{+/+}$ for the wild-type mice.

Genotyping by PCR and Northern blot analysis. In addition to Southern blotting, genomic PCR was applied for routine genotyping of littermates. For this purpose, three primers were designed for amplification of the mutant, wild-type, or both alleles in the same reaction. The primers were the following: p1, 5′-AGT GAT TTG AAG ACC AGC C-3′ (in intron 18); p2, 5′-GCC ACC AAA GAA CGG AGC-3′ (in the neomycin cassette); and p3, 5′-GGC TCC GTT CCT TTG CAG CAG-3′ (in exon 19). The PCR amplification was carried out in a 25-μl reaction mixture in the presence of 1× PCR buffer, 1× Q-buffer, 200 μM nucleotide mix, 1 μl of dimethyl sulfoxide, 0.6 U of *Taq* polymerase, and 8 pmol of each primer (QIAGEN, Valencia, CA). Amplification conditions consisted of 1 cycle at 94°C for 12 min, followed by 38 cycles of 45 s at 94°C, 45 s at 59°C, and 45 s at 72°C, with a final extension at 72°C for 10 min. The primer pair p1 and p3 produced a 430-bp wild-type allele, while p2 and p3 resulted in a 320-bp mutant allele (Fig. 1C). Both DNA fragments were generated from DNA of heterozygous animals.

Northern blot analysis was performed by isolating total RNA from *Abcc6*$^{+/+}$, *Abcc6*$^{+/-}$, and *Abcc6* $^{-/-}$ mouse livers using Trizol (Invitrogen Corp., Carlsbad, CA) per the manufacturer's protocols, followed by size separation using a 0.6 M formaldehyde–1% agarose gel under standard conditions. The RNA was transferred to nitrocellulose membrane by vacuum blotting and hybridized using a ^{32}P-labeled cDNA probe corresponding to exons 12 to 23 of *Abcc6* prepared by reverse transcription-PCR, followed by autoradiography using standard protocols (17).

Necropsy, histology, computed tomography (CT) scans, and transmission electron microscopy (TEM). Mice were euthanized in accordance with American Veterinary Medical Association guidelines (3), and necropsy was performed as previously described (40) using Tellyesniczky/Fekete fixative (70% [vol/vol] ethanol, 5% [vol/vol] glacial acetic acid, 4% [wt/vol] paraformaldehyde). The Institutional Animal Care and Use Committee approved all procedures using mice. Tissues and organs were further trimmed, paraffin embedded, sectioned (5 μm), and stained with hematoxylin-eosin using standard techniques. Several sections of the skin (dorsal and muzzle skin), eye, aorta, heart, and kidney were also stained for mineralization using the von Kossa stain procedure and alizarin red stain according to standard techniques (50). For visualization of glycosaminoglycans, colloidal iron stain was used.

For quantitation of tissue mineralization, computerized morphometric analysis of von Kossa-stained sections of muzzle skin was performed. Specifically, the sections were examined with a Nikon model TE2000 microscope (at a magnification of ×10) equipped with an AutoQuant Imaging system (Watervliet, New York, N.Y.). The numbers of vibrissae, both those with evidence of mineralization and those without, were determined in several fields, and the intensity of mineralization was expressed as pixels (arbitrary units) both per section and per individual mineralized vibrissa.

Samples for TEM were prepared using standard techniques as previously described (8). Briefly, mice were sacrificed, and selected tissues and organs were fixed in 4% paraformaldehyde, 2.5% glutaraldehyde, 0.1 M sodium cacodylate, pH 7.4, with 8.0 mM $CaCl_2$ for 2 h on ice. This was followed by postfixation with 1% osmium tetroxide for 1 h. After dehydration in a graded ethanol series followed by propylene oxide, the tissue was infiltrated and embedded in a mixture of Embed 812, nadic methyl anhydride, dodecenyl succinic anhydride, and DMP-30 (EM Sciences, Fort Washington, PA). Thick sections (1 μm) were cut and stained with methylene blue-azur blue for examination and selection of specific regions for further analysis. Thin sections were cut using a Leica UCT ultramicrotome and a diamond knife. Staining was with 2% aqueous uranyl acetate, or, alternatively, tissues were stained en bloc with 2% ethanolic uranyl acetate. Sections were examined and photographed at 80 kV using a Tecnai 12 transmission electron microscope equipped with a Gatan US1000 2K Ultrascan digital camera.

CT images were acquired with a MicroCAT II CT scanner (Imtek Inc., Knoxville, TN) using acquisition parameters of 40 kVp X-ray voltage, 500 μA anode current, 2,000-ms exposure time per source position, 180 rotational source positions, and a 4-by-4 bin factor for charge-coupled device imaging. Acquisition time was approximately 9 min per mouse. Images were reconstructed using the Feldkamp cone-beam algorithm to produce 100 μm^3 voxels in a 512- by 512- by 768-voxel volume. Mice were anesthetized with ketamine-xylazine prior to imaging to avoid motion artifacts.

Anti-Mrp6 antibody production and immunofluorescence. To generate anti-mouse Mrp6 antibody, the mouse *Abcc6* cDNA encoding amino acids 845 to 1010 (GenBank accession no. AX282516; gi 16609646) was generated using PCR techniques and cloned in frame with the glutathione *S*-transferase (GST) polypeptide cDNA at the EcoRI site of pGEX-4T-1 (Amersham Biosciences, Piscataway, NJ). A GST-Mrp6 fusion polypeptide was produced and purified following the manufacturer's protocol, except that the GST portion was not removed, and used to inoculate chickens. The polyclonal immunoglobulin G antibody was collected from chicken serum (Cocalico Biologicals, Inc., Reamstown, PA).

Tissue was frozen in Tissue-Tek optimal cutting temperature medium (Sakura Finetechnical Co., Ltd., Tokyo, Japan) for immunohistology, and 3-μm sections were cut, mounted on slides, and dried at room temperature for 30 min. Sections were fixed in methanol (−20°C for 5 min), dried as before, washed in phosphate-buffered saline, and blocked using 2.5% (wt/vol) bovine serum albumin fraction V. Chicken anti-mouse Mrp6 antibody was diluted 1:100 and placed on the slides for 1 h at room temperature. After being washed in phosphate-buffered saline, the bound antibody was detected using goat anti-chicken antibody labeled with fluorescein isothiocyanate (Molecular Probes, Inc., Eugene, OR) at a 1:300 dilution.

Using similar procedures, immunofluorescence microscopy was performed to analyze the components of the vibrissa capsule. The antielastin antibody (Elastin Products Company, Inc., Owensville, MO) was used at a dilution of 1:150, and the anti-type I collagen antibody (Rockland Immunochemicals, Inc., Gilbertsville, PA) was used at a dilution of 1:100. The primary immunoglobulin G antibodies were detected using a Texas Red-labeled anti-mouse secondary antibody.

RESULTS

Generation of mice with targeted inactivation of the *Abcc6* gene. The strategy to disrupt the *Abcc6* gene consisted of construction of a gene-targeting vector which contained an HSV-TK and neomycin cassette, resulting in replacement of 7.1 kb of mouse *Abcc6* DNA, including exons 15 to 18 and part of the flanking introns 14 and 18 (Fig. 1A). The targeting vector was electroporated into ES cells, and positive ES cell clones were selected by growth in medium containing the neomycin analog G418 and ganciclovir. Homologous recombination between the wild-type allele and targeted vector was confirmed by Southern blotting of SpeI digests with a probe corresponding to exons 12 and 13 (Fig. 1A). The wild-type allele resulted in a 5.5-kb SpeI fragment, while the targeted allele showed a fragment of 7.0 kb (Fig. 1B).

Three independently derived ES cell clones with a deletion of exons 15 to 18 were microinjected into C57BL/6J blastocysts, and chimeric males showed germ line transmission of the ES cell genome, as determined by agouti coat color of offspring from chimera C57BL/6J breedings. Two of these lines were extensively studied for the inheritance of the transgene using Southern analysis (Fig. 1B) or genomic PCR analysis (Fig. 1C) for their genotype and for pathological changes as reported below. In the initial litters from mating *Abcc6*$^{+/-}$ mice, 35 pups were born, and among them 8 pups were *Abcc6*$^{+/+}$, 17 were

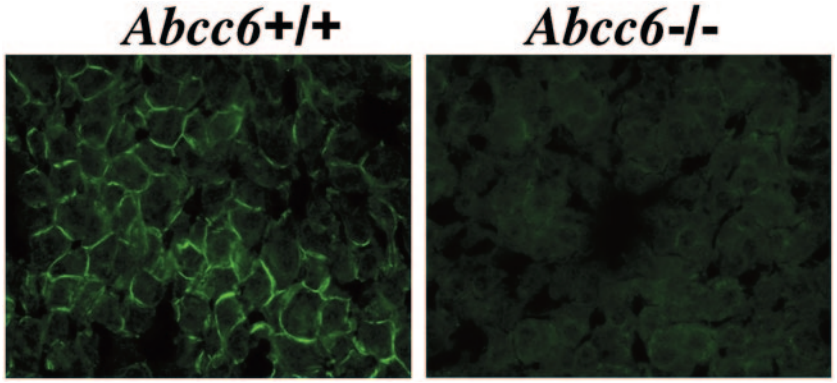

FIG. 2. Immunofluorescence of the liver in wild-type (+/+) animals and in *Abcc6*$^{-/-}$ mice using a chicken anti-mouse Mrp6 antibody. Note the presence of Mrp6 at hepatocytes in control liver (left panel), while no signal is seen in the liver from *Abcc6*$^{-/-}$ mice. Original magnification, ×400.

Abcc6$^{+/-}$, and 10 were *Abcc6*$^{-/-}$. The *Abcc6* genotype distribution (0.91:1.94:1.14) does not deviate significantly from the expected Mendelian 1:2:1 ratio of wild-type:heterozygous:null (χ^2, $P > 0.05$). These results indicated that Mrp6 deficiency does not cause embryonic lethality of *Abcc6*$^{-/-}$ mice during gestation.

Total RNA was then extracted from the livers of *Abcc6*$^{+/+}$, *Abcc6*$^{+/-}$, and *Abcc6*$^{-/-}$ mice and subjected to Northern blot analysis (Fig. 1D). An approximately 5-kb mRNA species corresponding to the mouse *Abcc6* mRNA was detected in the +/+ and +/− lanes using an *Abcc6* cDNA probe, while no *Abcc6* mRNA was detected in the −/− sample.

To confirm that the *Abcc6*$^{-/-}$ mice were negative for Mrp6 expression, the liver from the wild-type and null mice was subjected to immunofluorescence with an antibody recognizing mouse Mrp6. As reported previously (47), Mrp6 was expressed in the basolateral membranes of the wild-type mouse hepatocytes (Fig. 2, left panel). In contrast, immunofluorescence for Mrp6 in the *Abcc6*$^{-/-}$ mice was entirely negative (Fig. 2, right panel).

Mineralization of connective tissues in *Abcc6*$^{-/-}$ mice. The *Abcc6*$^{-/-}$ mice appeared healthy and were fertile, and initial examination of the back skin, by visual inspection following depilitation or by diagnostic skin biopsy, did not reveal any apparent phenotype. Subsequently, complete necropsies were done using standardized phenotyping methods on a total of 18 mice ranging in age from 428 to 454 days (the distribution of phenotypes for females was two +/+, three +/−, and two −/−; the distribution of phenotypes for males was three +/+, four +/−, and four −/−). In addition, male and female heterozygotes at 569 days and one null male at 793 days of age were examined. A variety of aging changes were evident in all mice, including preputial and clitoral gland ductal ectasia with glandular atrophy, cementum hyperplasia of molars, mild acidophilic macrophage pneumonia, mild focal chronic inflammation of the Harderian and salivary glands, splenic melanosis, various degrees of chronic interstitial nephritis, and other changes.

Pathological lesions were found exclusively in the *Abcc6*$^{-/-}$ mice. Specifically, examination of hematoxylin-eosin-stained sections revealed profound mineralization of a number of tissues, including the capsule surrounding the sinuses of vibrissae, the walls of medium-sized arteries, and a variety of other tissues, including the skin, retina, kidney, interscapular brown fat, and in one case the seminiferous tubules of the testicle of a male mouse (Fig. 3 and 4). Particularly striking was the mineralization of the vibrissae, as confirmed by von Kossa and alizarin red stains (Fig. 4F and I). Colloidal iron stain used for detection of glycosaminoglycans did not show differences in the skin between the *Abcc6*$^{-/-}$ and *Abcc6*$^{+/+}$ mice (not shown). It should be reemphasized that mineralization of the affected tissues was noted only in *Abcc6*$^{-/-}$ mice, and no evidence of such a process was observed in +/− or +/+ mice. It should be noted that the mineral deposition in the affected tissues was patchy, and certain tissues, such as the lung and the liver, did not show any evidence of mineralization.

To evaluate the extent of tissue mineralization, a total body CT scan was performed on an *Abcc6*$^{+/+}$ and *Abcc6* $^{-/-}$ mouse. Computerized reconstruction of the *Abcc6*$^{-/-}$ mouse revealed densities suggestive of mineralization in the dermis, kidneys, and the subcutaneous tissues in a patchy pattern. Specifically, in the skin, a total of 14 foci of mineralization, <0.5 mm^3 in size and with an average size of 0.12 mm^3, were detected (Fig. 5). In addition, four foci of mineralization with an average size of 0.05 mm^3 were detected in the kidneys. No evidence of soft tissue mineralization was noted in the control mouse of the same age (Fig. 5).

To examine the mineralization process in further detail, skin biopsies from the muzzle area were processed for TEM. Examination of the connective tissue demonstrated areas of mineralization associated with both collagen fibrils and elastic fibers (Fig. 6). Relatively large areas of electron-dense material corresponding to the mineralized regions were observed. Ultrastructural detail in the central portions of the mineralized regions was obscured by the electron density. However, at the periphery of the regions, the mineralization of collagen fibrils and elastic fibers was observed. A mineralization of collagen fibrils was visualized in transverse section (Fig. 6A and B). Aggregates of collagen fibrils were observed associated with mineralized material. In the central portion the electron density all but obscured fibril structure. At the periphery, single or small groups of fibrils were observed with various amounts of electron density. As the fibrils became more mineralized, they were seen associated with larger aggregates, suggesting that

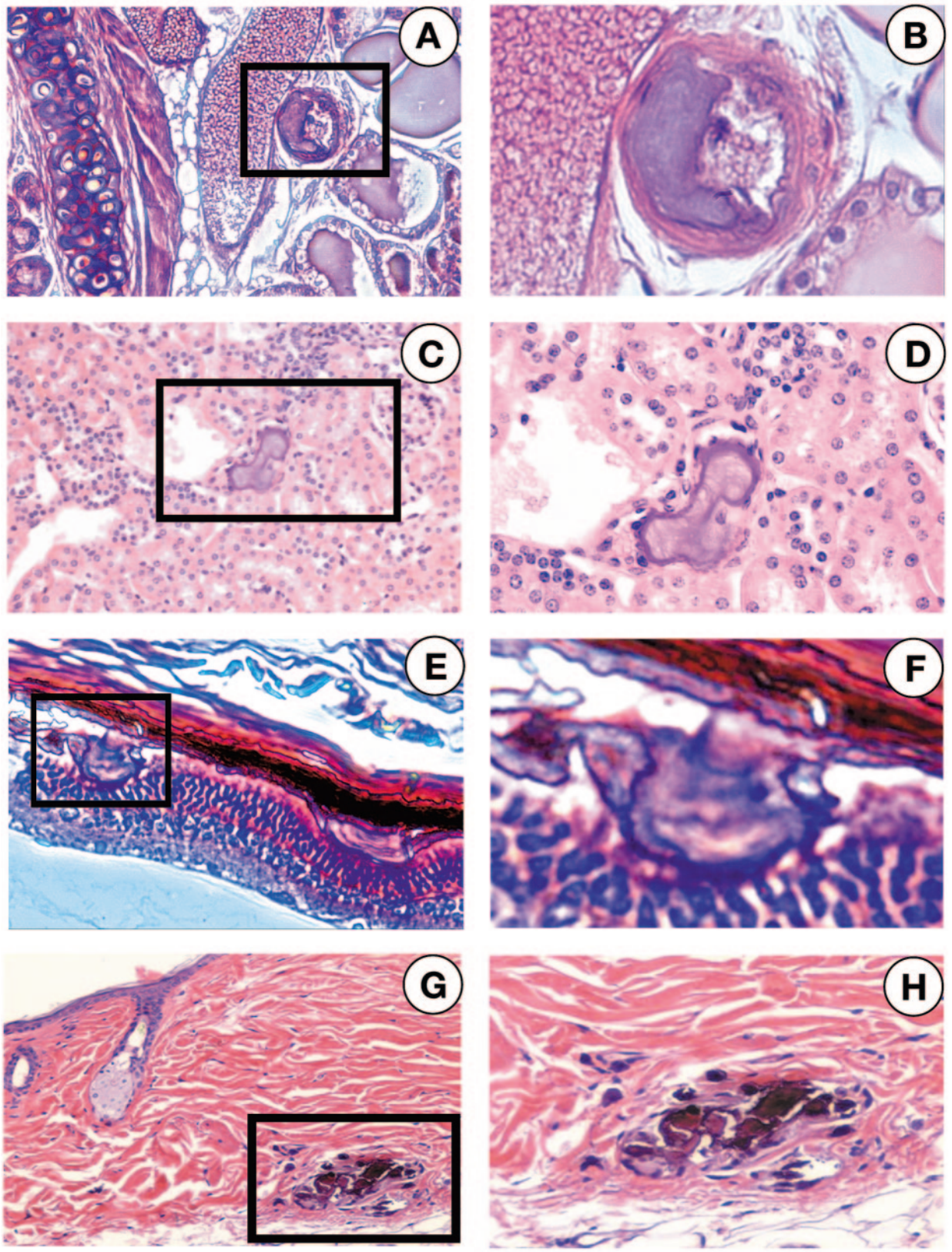

FIG. 3. Histopathologic evidence of ectopic mineralization in *Abcc6* null mice. Mid-sized arterial blood vessel in the hind leg (A and B), renal tubule (C and D), drusen in the retina (E and F), and dermis (G and H). The pictures in the left column show low magnification, and the areas boxed are shown in higher magnification in the right column. Hematoxylin-eosin staining was used.

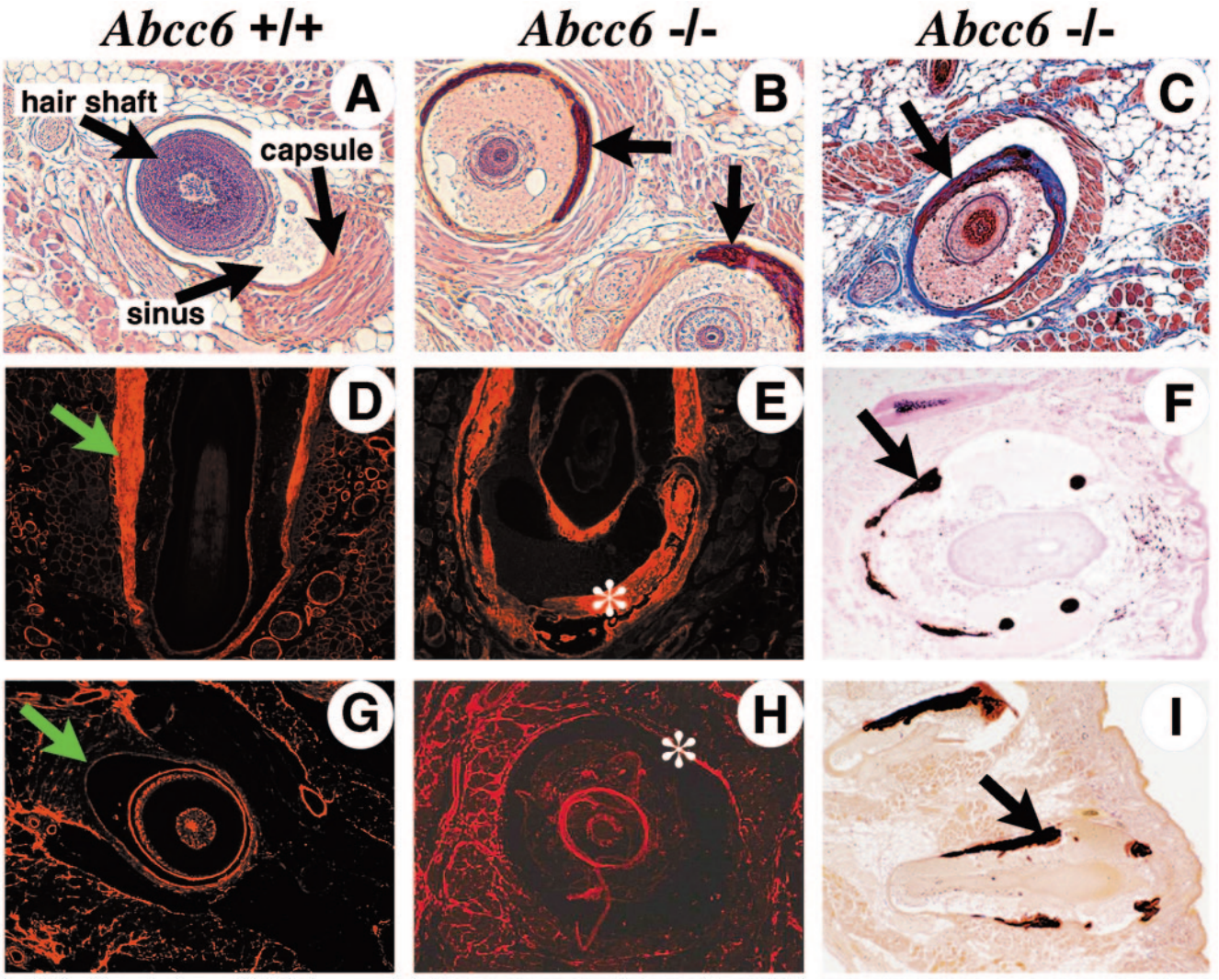

FIG. 4. Demonstration of ectopic mineralization of the vibrissae in *Abcc6* null mice. (A) Histopathology of the $Abcc6^{+/+}$ mouse reveals the presence of a large hair shaft of vibrissae surrounded by a blood vessel sinus which is encased by a capsule. Histopathologic stain by hematoxylin-eosin (B) or trichrome (C) stains suggests mineralization of the fibrous capsule in $Abcc6^{-/-}$ mice (arrows). von Kossa (F) and alizarin red (I) stains confirm mineralization (arrows). Characterization of the capsule of vibrissae in $Abcc6^{+/+}$ mice by immunofluorescence for type I collagen (D) or for elastin (G) with specific antibodies reveals the presence of these connective tissue components (arrows). Immunofluorescence of the corresponding areas in $Abcc6^{-/-}$ mice reveals that the mineralization process is associated with type I collagen (E) and elastin (H) within the connective tissue capsule of the vibrissae (asterisks).

increasing mineralization is associated with fibril aggregation. In addition, distinct mineralization of elastic fibers was also observed (Fig. 6C and D). The mineralization of elastic fibers was particularly dense at the periphery of the fiber, apparently rich in microfibrillar components.

Since extensive tissue mineralization, such as noted in $Abcc6^{-/-}$ mice, could reflect metastatic mineralization due to hypercalcaemia, the serum calcium, phosphorus, and protein levels in the $Abcc6^{+/+}$, $Abcc6^{+/-}$, and $Abcc6^{-/-}$ mice were determined by routine clinical laboratory procedures. As shown in Table 1, no significant differences in these laboratory parameters were noted. Comprehensive metabolic panel, including liver function tests and serum creatinine, also yielded results within the normal range (not shown).

Collectively, these data demonstrate extensive aberrant mineralization of soft tissues in organs affected by PXE, namely, the skin, arterial blood vessels, and the eyes. Similar to results in patients with PXE (32), the calcium and phosphorus serum values are normal. Thus, these mice recapitulate features of PXE.

Mineralization of the connective tissue capsule of vibrissae as an early biomarker of disease in $Abcc6^{-/-}$ mice. A particularly striking finding in the mice initially necropsied at the age of ~430 days or older was marked mineralization of the vibrissa sinus capsule. This capsule was suggested to consist of connective tissue and could be thought to provide clues to the mineralization process. An evaluation of the biochemical nature of the capsule in wild-type mice by specific histopathologic stains and immunohistochemistry was performed. First, the capsule was shown to be clearly positive with trichrome stain

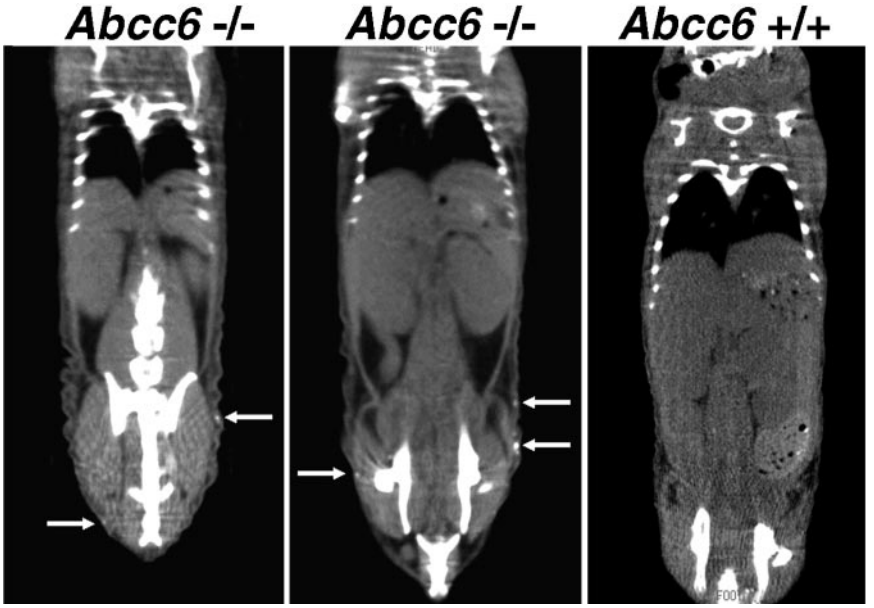

FIG. 5. CT scan of an *Abcc6*$^{-/-}$ mouse reveals the presence of foci of mineralization in the skin (arrows). The two optical sections are representative of the entire CT scan, which revealed a total of 14 mineralized foci (average size, 0.12 mm^3) in the dermis of this *Abcc6*$^{-/-}$ mouse. No evidence of similar mineralization was observed in an age-matched control mouse (*Abcc6*$^{+/+}$).

for collagen (Fig. 4C), and immunofluorescence with an anti-type I collagen antibody confirmed the presence of this connective tissue protein (Fig. 4D). Second, immunofluorescence with an antielastin antibody demonstrated a narrow, yet well-defined layer of elastin within the capsule (Fig. 4G). In contrast, smooth muscle actin expression was entirely negative, while adjacent arterial blood vessels were clearly positive serving as a positive control (not shown). Immunofluorescence of *Abcc6*$^{-/-}$ mice, with the same antibodies, revealed that the mineralization process affected the layers containing type I collagen and elastin (Fig. 4E and H), consistent with the findings by TEM. Thus, the capsule consists of connective tissue, containing at least type I collagen and elastin.

Secondly, since mineralization of the connective tissue capsule of the vibrissae was a prominent and consistent feature in the *Abcc6*$^{-/-}$ mice, we postulated that this finding would serve as an early biomarker of the pathological process affecting the arteries and the retina. To test this hypothesis, biopsies of muzzle skin containing vibrissae of *Abcc6*$^{-/-}$ mice of various ages were taken. Mineralization was detected in some mice at 5 weeks of age, while this process was consistently evident in *Abcc6* null mice at 6 weeks old (Fig. 7). None of the mice studied at 3 weeks of age showed any histologic evidence of mineralization (not shown).

Finally, to quantitate the progressive nature of the mineralization process, tissue sections of muzzle skin containing vibrissae from *Abcc6*$^{-/-}$ and *Abcc6*$^{+/+}$ mice of different ages were stained with von Kossa stain and analyzed by computerized morphometry. No calcification of vibrissae was noted in wild-type control mice, while the degree of calcification progressively increased when *Abcc6*$^{-/-}$ mice of 1.5, 6, and 22 months of age were compared (Fig. 7 and Table 2). Specifically, the total area of calcification per μm^2 area of tissue section increased almost 10-fold between 1.5 and 6 months of age and further doubled when the mice reached the age of 22 months (Table 2). At the same time, the degree of mineralization of individual vibrissae affected by the process increased 6.5-fold when the *Abcc6*$^{-/-}$ mice advanced in age from 1.5 to 22 months. Collectively, the mineralization of vibrissae is detectable at 5 to 6 weeks of age, and it progressively increases, potentially reflecting the mineralization process affecting a number of tissues.

DISCUSSION

The human *ABC* gene family contains an estimated 48 members divided into seven subgroups (for review, see references 13 and 14). The *ABCC* subgroup consists of 12 members with 9 members encoding MRPs and 3 members encoding ion channel proteins or regulators of potassium channels. Deleterious mutations in the *ABCC* genes have been linked to several heritable human diseases. *ABCC2* (*CMOAT*) was associated with Dubin-Johnson syndrome (hyperbilirubinemia II; OMIM 237500), and *ABCC3* expression is enhanced in Dubin-Johnson syndrome patients. Mutations in *ABCC7* leads to cystic fibrosis (OMIM 219700), and, consequently, this gene is better known as the cystic fibrosis transmembrane conductance receptor gene *CFTR*. *ABCC8* mutations are found in patients with familial persistent hyperinsulinemic hypoglycemia of infancy (or nesidioblastosis of the pancreas; OMIM 256450 and 600509) and autosomal dominant type II diabetes (OMIM 600509) (22, 23). *ABCC9* mutations are associated with dilated cardiomyopathy with ventricular tachycardia (OMIM 608569) (7). *ABCC10*, *ABCC11*, and *ABCC12* genes are not well characterized, but it was proposed that *ABCC11* and *ABCC12* may be potential gene candidates for paroxysmal kinesigenic choreoathetosis (OMIM 128200) and infantile convulsions with paroxysmal choreoathetosis (OMIM 602066) (58). All of the

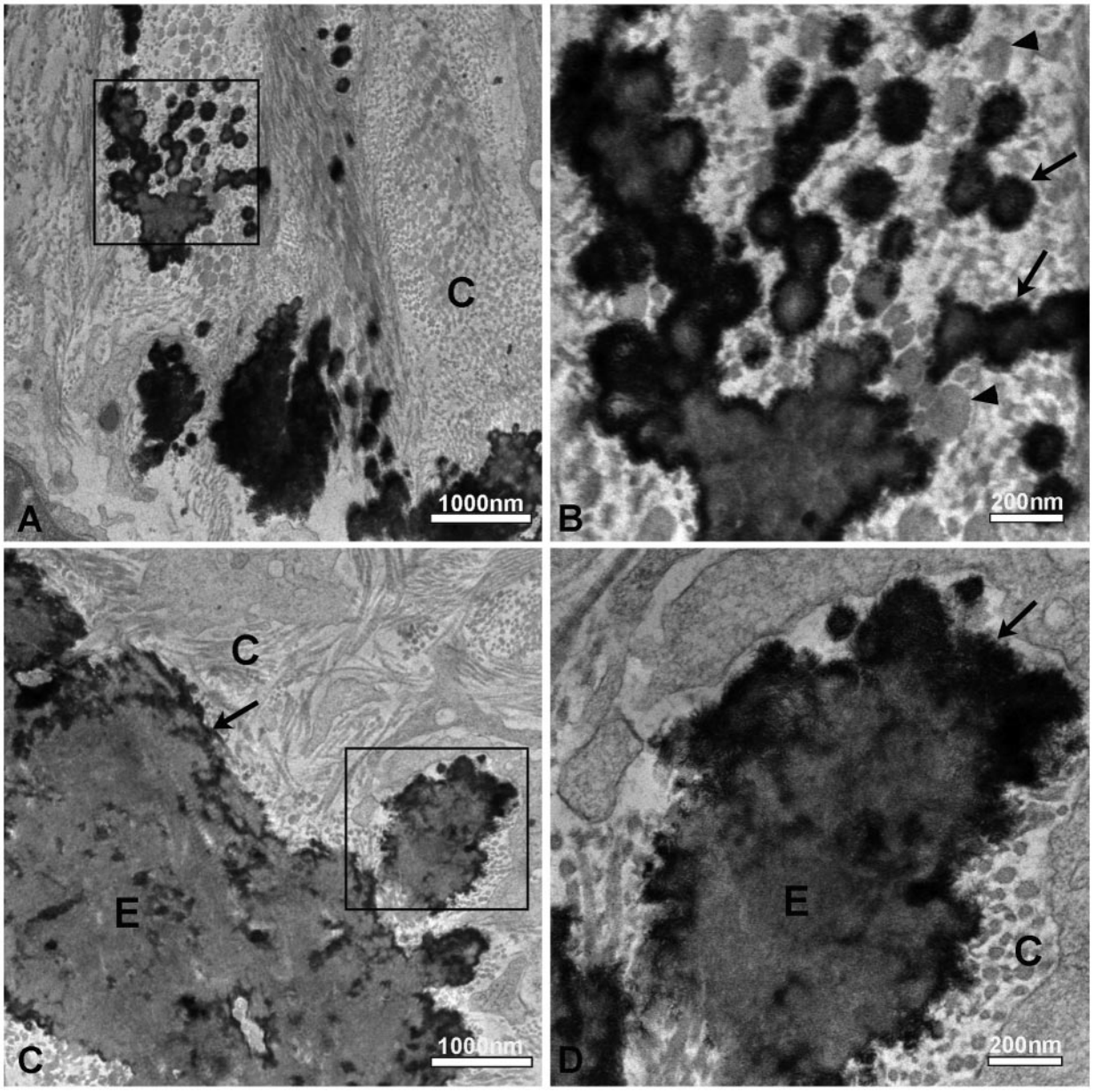

FIG. 6. TEM of connective tissue in the area of the vibrissa capsule reveals mineralization of both collagen and elastic structures in *Abcc6*$^{-/-}$ mice. Panels are labeled A to D in the lower-left corners. In the panels, C indicates areas containing collagen and E indicates areas containing elastin. Dense deposits of mineral are noted amid collagen fibers in panel A, and higher magnification of the boxed area, shown in panel B, reveals distinct mineralization of collagen fibers seen in the transverse section (arrows) and also the cauliflower collagen fiber morphology (arrowhead) typically observed in the dermis of PXE patients. Distinct mineralization is noted at the periphery of an area apparently representing elastic structures in panel C, and higher magnification of the boxed area, shown in panel D, reveals diffuse mineralization.

human *ABCC* gene family members have mouse homologues except for *ABCC11*, which may have arisen as a recent duplication of *ABCC12* (51). Thus, the mouse presents an excellent animal model system for the study of *Abcc* genes, as highlighted here for *Abcc6*.

The *Abcc6* null mouse develops a mineralization phenotype similar to that of PXE patients. Specifically, both the *Abcc6* null mice and PXE patients manifest with ectopic mineralization in the skin, eye, kidney, and arterial blood vessels. This kind of generalized mineralization defect, while rarely seen in the eyes of some mouse mutants, is highly unusual, based on systemic analysis of a large number of mutant mice at The Jackson Laboratory (56, 57). Furthermore, although mineralized lesions in the kidney may not be uncommon in strains prone to calcification, their presence in mouse strains not prone to calcification is significant (J. P. Sundberg, unpublished observations). Collectively, the *Abcc6*$^{-/-}$ mice display generalized, ectopic mineralization reminiscent of that in PXE. However, some differences were also noted between the Mrp6-deficient mice and PXE patients. For example, the PXE-asso-

TABLE 1. Calcium and phosphorus levels in the serum of *Abcc6* wild-type, heterozygous, and null mice

Parameter	Value (mean ± SD) in:		
	WT (+/+) mice ($n = 7$)[a]	Heterozyous (+/−) mice ($n = 7$)[b]	Null (−/−) mice ($n = 9$)[b]
Calcium (mg/dl)	10.1 ± 0.7	9.5 ± 1.2	9.3 ± 1.5
Phosphorus (mg/dl)	12.9 ± 1.6	12.2 ± 2.0	10.8 ± 2.2
Ca/P ratio	0.79 ± 0.10	0.79 ± 0.08	0.88 ± 0.14
Protein (g/dl)	5.0 ± 0.3	4.6 ± 0.3	5.0 ± 0.4

[a] WT, wild type.
[b] The values are not statistically different from WT controls.

TABLE 2. Quantitation of mineralization of vibrissae in *Abcc6*$^{-/-}$ mice of different ages[a]

Mouse[b]	Age (mo.)	No. of vibrissae examined (no. mineralized/total)	Total area of mineralization		Area of mineralization per affected vibrissa	
			U × 10^3[c]	Fold[d]	U × 10^3[c]	Fold[d]
WT	6	0/9				
KO	1.5	3/9	16.1	1.0	5.6	1.0
KO	6	10/10	157.3	9.8	15.7	2.8
KO	22	8/9	292.9	18.2	36.6	6.5

[a] Skin sections stained with von Kossa stain were examined by computerized morphometric analyses (see Materials and Methods).
[b] WT, wild-type (*Abcc6*$^{+/+}$) control; KO, knockout (*Abcc6*$^{-/-}$) mice.
[c] Units are expressed as pixels per μm^2 reflecting the intensity of von Kossa stain, as illustrated in Fig. 7.
[d] Calculated using the 1.5-month-old knockout mouse as 1.0.

ciated manifestations were consistent in *Abcc6* null mice but are quite variable in PXE patients. This difference may be due to greater genetic homogeneity and a common environment and diet in the mouse versus the human population. Further analysis of *Abcc6* null mice may reveal greater heterogeneity in the symptoms upon changing the genetic background of the mouse, environmental factors, and diet, thus possibly providing an explanation for the diversity of PXE manifestations in humans.

Affected skin of PXE patients is characterized by the accumulation of abnormal elastotic material, which progressively mineralizes in the middermis, resulting in formation of papules. The cutaneous areas most commonly affected in humans are the neck, the antecubital, popliteal, and axillary fossae, and the inguinal and periumbilical regions with yellowish papules coalescing to form redundant, lax skin. Skin papules, with distinct mineralization, which was also visualized by computed tomography, were seen on 18-month-old *Abcc6* null mice. However, the mineralized loci in the mice were found over the rump instead of the corresponding affected areas in humans, and they were relatively small (<0.5 mm^3) and widely spaced. An explanation for this difference may be that mouse skin has much lower amounts of elastic fibers compared to human skin (26). Also, papule formation in humans occurs primarily at flexural sites, i.e., areas of wear and tear, and may be exposed to UV light leading to dermal damage with subsequent repair resulting in greater elastin deposition and eventual mineralization. The laboratory housing conditions and dense fur prevent damaging UV exposure to mouse skin. An interesting finding was the ubiquitous mineralization of the outer connective tissue sheaths of vibrissae in the *Abcc6* null mice. Immunohistochemical analysis of the vibrissa sheath revealed abundant type I collagen as well as elastic structures that may serve as sites for mineralization. Mineralization of the vibrissa sheath was noted as early as the fifth week of life and was shown to increase progressively as determined by computerized morphometric analyses. Thus, mineralization of vibrissae may serve as a means to monitor the *Abcc6* null mice and therefore provides a biomarker of the onset and progress of the disease processes leading to PXE. Electron microscopy of the skin revealed not only the mineralization of elastic fibers but also that of collagen fibers. While PXE is often described as mineralization of elas-

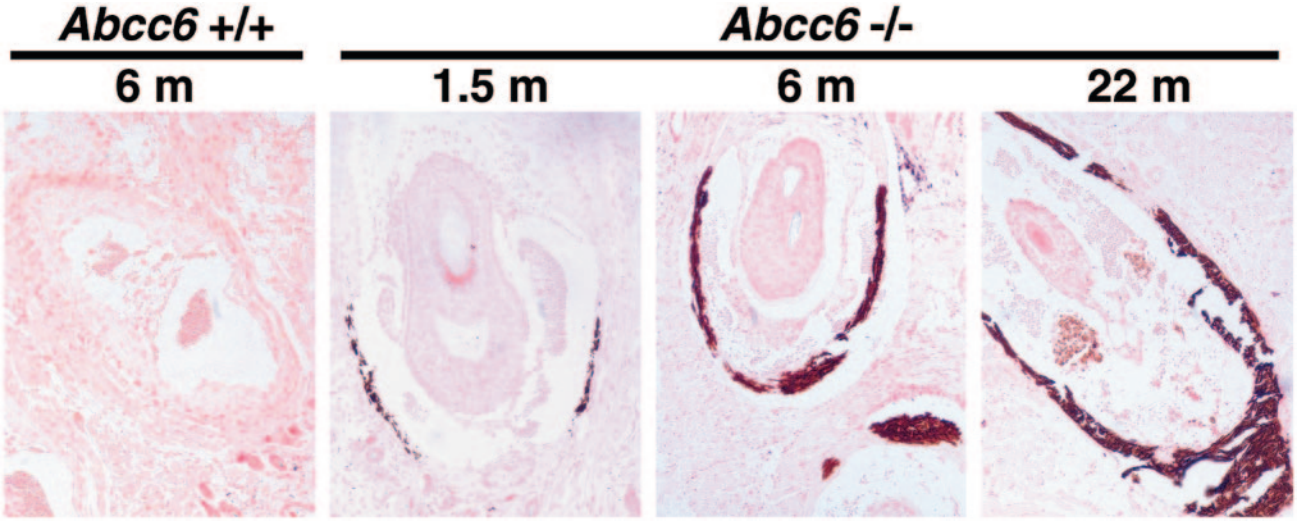

FIG. 7. Demonstration that the mineralization process affecting the vibrissae of *Abcc6*$^{-/-}$ mice is progressive. Sections of muzzle skin from a 6-month old *Abcc6*$^{+/+}$ mouse, as well as from *Abcc6*$^{-/-}$ mice of 1.5 months, 6 months, and 22 months of age were stained with von Kossa stain. While no mineralization is noted in the *Abcc6*$^{+/+}$ mouse, there is a progressive increase in mineralization with advancing age of *Abcc6*$^{-/-}$ mice. This progression was quantitated by computerized morphometric analysis (Table 2).

tin, mineralized collagen fibers were observed in PXE patients (16, 18, 20, 32, 34), very similar to the findings in *Abcc6* null mice.

Mineral deposits were observed in the intermediate-sized arterial vessels of the hind legs. In humans, mineralization of the arterial blood vessels in the lower legs leads to intermittent claudication, and the *Abcc6* null mice are currently undergoing testing for this condition. Deposits in the coronary arteries or gastric vessels were not observed in *Abcc6* null mice but are typical in humans with PXE, leading occasionally to coronary infarction or blood vessel rupture. Perhaps the PXE-associated arteriosclerosis of these blood vessels in humans is not solely due to the lack of MRP6 function but may be due to, or exacerbated by, other genes, the environment, or diet. The majority of the *Abcc6* null mice appeared healthy up to 22 months of age, although there were a few sporadic sudden deaths that may have been due to cardiovascular complications.

Mineralization of the eye was associated with the retina which contains the elastin-rich Bruch's membrane. It is unclear at this point whether the mice develop loss of visual acuity and possible development of angioid streaks, features of ophthalmologic findings in PXE (48, 65).

Several of the mice displayed mineral deposits in the kidney as visualized by histopathologic examinations and by scan, but these deposits were small and few. In some cases, small renal deposits have been described in PXE patients using sonography (12, 55). However, similar deposits were detected in non-PXE patients (15), and there are reported cases of patients with renal failure or undergoing dialysis who have developed PXE-like symptoms (33, 35, 46). Thus, in humans, typical PXE-associated mineralizations may be exacerbated by a compromised renal system. Although the kidney has much lower levels of *Abcc6* mRNA than the liver, it is readily detectable by reverse transcription-PCR and by in situ hybridization (4), and thus *Abcc6* expression in kidneys may have an important role in regulating mineralization.

The transport substrates for several of the ABCC proteins have been determined. MRP1, 2, and 3 (*ABCC1*, *ABCC2*, and *ABCC3*, respectively) confer resistance to natural product anticancer agents and methotrexate, and they are also known to transport glutathione and glucuronate conjugates and organic anions (for a review, see references 21 and 27). MRP4 (*ABCC4*) and MRP5 (*ABCC5*) confer resistance to nucleotide analogs, and MRP4 can also transport glucuronate conjugates and methotrexate (for a review, see reference 45). *CFTR* (*ABCC7*) encodes a chloride ion channel transporter (39). *SUR1* (*ABCC8*) and *SUR2* (*ABCC9*) bind sulfonylurea and regulate potassium channels involved in modulating insulin levels (37). The *ABCC13* gene, although transcribed, encodes a truncated protein that probably lacks transporter activity (2, 64). The transport substrates of the other *ABCC* genes are not well characterized.

As *ABCC6* encodes an MRP-like protein, transport studies have so far focused on typical MRP protein substrates, such as glutathione conjugates and anticancer drugs. Vesicle-loading and ex vivo studies using rat and human MRP6 test systems demonstrated transport of the cyclic pentapeptide, endothelein receptor antagonist BQ123 (5, 31). Interestingly, the rat MPR6 failed to transport glutathione conjugates (31), but these compounds were readily transported by the human MRP6 (5, 24). Human MRP6 was also shown to be a weak transporter of anticancer agents (5). The in vivo MRP6 substrate has remained elusive, and its discovery will provide an essential key to understanding the pathophysiology of PXE.

Mouse models for *Abcc* gene deficiency generated by gene-targeting strategies include *Abcc1* (30, 63), *Abcc7* (for a review, see reference 19), *Abcc8* (49, 52), and *Abcc9* (11), and a spontaneous frameshift mutation in *Abcc2* was found in a rat line (TR^-) (25, 36). The phenotypes generated by these gene ablations varied greatly from immune impairment and abnormal drug metabolism (*Abcc1*), hyperbilirubinemia (*Abcc2*), cystic fibrosis-like symptoms (*Abcc7*), and mild, transitory hypo- and hyperglycemia (*Abcc8* and *Abcc9*), but none of these animal models demonstrated abnormal mineralization of soft tissues as in the *Abcc6* null mice. This broad spectrum of phenotypes demonstrates the diversity of physiological roles for the ABC subfamily and also suggests a unique transport function for MRP6 that is not compensated for by other ABC transporters. In many of these animal models, there is a direct correlation between the site of gene expression and the location of lesions. Hence, organs or tissues that are affected in *Abcc* null animals also express high levels of the corresponding *Abcc* gene in wild-type animals. An exception to this rule is *Abcc6*: neither *Abcc6* null mice nor PXE patients have an apparent liver disease, yet the liver both in humans and mice generates the greatest levels of MRP6 protein and mRNA. These observations suggest that PXE is a metabolic disorder at the environment-genome interface (62). However, this does not negate the possibility that low-level expression of *Abcc6* in other tissues has an important physiological role (4).

This study demonstrated that the *Abcc6* null mouse can serve as a model for PXE, providing a crucial animal system to elucidate PXE pathomechanisms and to test therapeutic interventions. Further, these mice may serve as a general model of mineralization in studies of vascular and ocular degeneration.

ACKNOWLEDGMENTS

Carol Kelly assisted in preparation of the manuscript. We thank James Miller, Kaitlin Petrella, Chris Cardi, Mark Pawlowsky, and Joya Sahu for technical assistance. Madhukar Thakur assisted in the interpretation of the CT data, and John Farber and Jason B. Lee provided helpful discussion on pathology.

This study was supported by NIH/NIAMS grants R01AR38923 and R01AR52627.

REFERENCES

1. **Abbondanzo, S. J., I. Gadi, and C. L. Stewart.** 1993. Derivation of embryonic stem cell lines. Methods Enzymol. **225:**803–823.
2. **Annilo, T., and M. Dean.** 2004. Degeneration of an ATP-binding cassette transporter gene, ABCC13, in different mammalian lineages. Genomics **84:** 34–46.
3. **AVMA Panel on Euthanasia. American Veterinary Medical Association.** 2001. 2000 Report of the AVMA Panel on Euthanasia. J. Am. Vet. Med. Assoc. **218:**669–696.
4. **Beck, K., K. Hayashi, B. Nishiguchi, O. Le Saux, M. Hayashi, and C. D. Boyd.** 2003. The distribution of *Abcc6* in normal mouse tissues suggests multiple functions for this ABC transporter. J. Histochem. Cytochem. **51:** 887–902.
5. **Belinsky, M. G., Z. S. Chen, I. Shchaveleva, H. Zeng, and G. D. Kruh.** 2002. Characterization of the drug resistance and transport properties of multidrug resistance protein 6 (MRP6, ABCC6). Cancer Res. **62:**6172–6177.
6. **Belinsky, M. G., and G. D. Kruh.** 1999. MOAT-E (ARA) is a full-length MRP/cMOAT subfamily transporter expressed in kidney and liver. Br. J. Cancer **80:**1342–1349.
7. **Bienengraeber, M., T. M. Olson, V. A. Selivanov, E. C. Kathmann, F. O'Cochlain, F. Gao, A. B. Karger, J. D. Ballew, D. M. Hodgson, L. V.**

Zingman, Y. P. Pang, A. E. Alekseev, and A. Terzic. 2004. *ABCC9* mutations identified in human dilated cardiomyopathy disrupt catalytic KATP channel gating. Nat. Genet. **36:**382–387.
8. **Birk, D. E., and R. L. Trelstad.** 1986. Extracellular compartments in tendon morphogenesis: collagen fibril, bundle, and macroaggregate formation. J. Cell Biol. **103:**231–240.
9. **Borst, P., R. Evers, M. Kool, and J. Wijnholds.** 1999. The multidrug resistance protein family. Biochim. Biophys. Acta **1461:**347–357.
10. **Chassaing, N., L. Martin, J. Mazereeuw, L. Barrie, S. Nizard, J. L. Bonafe, P. Calvas, and A. Hovnanian.** 2004. Novel *ABCC6* mutations in pseudoxanthoma elasticum. J. Investig. Dermatol. **122:**608–613.
11. **Chutkow, W. A., V. Samuel, P. A. Hansen, J. Pu, C. R. Valdivia, J. C. Makielski, and C. F. Burant.** 2001. Disruption of Sur2-containing K(ATP) channels enhances insulin-stimulated glucose uptake in skeletal muscle. Proc. Natl. Acad. Sci. USA **98:**11760–11764.
12. **Crespi, G., L. E. Derchi, and S. Saffioti.** 1992. Sonographic detection of renal changes in pseudoxanthoma elasticum. Urol. Radiol. **13:**223–225.
13. **Dean, M., Y. Hamon, and G. Chimini.** 2001. The human ATP-binding cassette (ABC) transporter superfamily. J. Lipid Res. **42:**1007–1017.
14. **Dean, M., A. Rzhetsky, and R. Allikmets.** 2001. The human ATP-binding cassette (ABC) transporter superfamily. Genome Res. **11:**1156–1166.
15. **Domjan, J. M., and K. C. Dewbury.** 1996. Case report: multiple highly reflective foci in the renal parenchyma are not specific for pseudoxanthoma elasticum. Br. J. Radiol. **69:**871–872.
16. **Eng, A. M., and J. Bryant.** 1975. Clinical pathologic observations in pseudoxanthoma elasticum. Int. J. Dermatol. **14:**586–605.
17. **Gheduzzi, D., R. Guidetti, C. Anzivino, P. Tarugi, E. Di Leo, D. Quaglino, and I. P. Ronchetti.** 2004. *ABCC6* mutations in Italian families affected by pseudoxanthoma elasticum (PXE). Hum. Mutat. **24:**438–439.
18. **Gheduzzi, D., R. Sammarco, D. Quaglino, L. Bercovitch, S. Terry, W. Taylor, and I. P. Ronchetti.** 2003. Extracutaneous ultrastructural alterations in pseudoxanthoma elasticum. Ultrastruct. Pathol. **27:**375–384.
19. **Grubb, B. R., and R. C. Boucher.** 1999. Pathophysiology of gene-targeted mouse models for cystic fibrosis. Physiol. Rev. **79:**S193–214.
20. **Hausser, I., and I. Anton-Lamprecht.** 1991. Early preclinical diagnosis of dominant pseudoxanthoma elasticum by specific ultrastructural changes of dermal elastic and collagen tissue in a family at risk. Hum. Genet. **87:**693–700.
21. **Homolya, L., A. Varadi, and B. Sarkadi.** 2003. Multidrug resistance-associated proteins: Export pumps for conjugates with glutathione, glucuronate or sulfate. Biofactors **17:**103–114.
22. **Huopio, H., T. Otonkoski, I. Vauhkonen, F. Reimann, F. M. Ashcroft, and M. Laakso.** 2003. A new subtype of autosomal dominant diabetes attributable to a mutation in the gene for sulfonylurea receptor 1. Lancet **361:**301–307.
23. **Huopio, H., F. Reimann, R. Ashfield, J. Komulainen, H. L. Lenko, J. Rahier, I. Vauhkonen, J. Kere, M. Laakso, F. Ashcroft, and T. Otonkoski.** 2000. Dominantly inherited hyperinsulinism caused by a mutation in the sulfonylurea receptor type 1. J. Clin. Investig. **106:**897–906.
24. **Ilias, A., Z. Urban, T. L. Seidl, O. Le Saux, E. Sinko, C. D. Boyd, B. Sarkadi, and A. Varadi.** 2002. Loss of ATP-dependent transport activity in pseudoxanthoma elasticum-associated mutants of human *ABCC6* (MRP6). J. Biol. Chem. **277:**16860–16867.
25. **Jansen, P. L., W. H. Peters, and W. H. Lamers.** 1985. Hereditary chronic conjugated hyperbilirubinemia in mutant rats caused by defective hepatic anion transport. Hepatology **5:**573–579.
26. **Johnston, K. J., A. I. Oikarinen, N. J. Lowe, J. G. Clark, and J. Uitto.** 1984. Ultraviolet radiation-induced connective tissue changes in the skin of hairless mice. J. Investig. Dermatol. **82:**587–590.
27. **Kruh, G. D., and M. G. Belinsky.** 2003. The MRP family of drug efflux pumps. Oncogene **22:**7537–7552.
28. **Kwee, L., H. S. Baldwin, H. M. Shen, C. L. Stewart, C. Buck, C. A. Buck, and M. A. Labow.** 1995. Defective development of the embryonic and extraembryonic circulatory systems in vascular cell adhesion molecule (VCAM-1) deficient mice. Development **121:**489–503.
29. **Le Saux, O., K. Beck, C. Sachsinger, C. Silvestri, C. Treiber, H. H. Goring, E. W. Johnson, A. De Paepe, F. M. Pope, I. Pasquali-Ronchetti, L. Bercovitch, A. S. Marais, D. L. Viljoen, S. F. Terry, and C. D. Boyd.** 2001. A spectrum of *ABCC6* mutations is responsible for pseudoxanthoma elasticum. Am. J. Hum. Genet. **69:**749–764.
30. **Lorico, A., G. Rappa, R. A. Finch, D. Yang, R. A. Flavell, and A. C. Sartorelli.** 1997. Disruption of the murine MRP (multidrug resistance protein) gene leads to increased sensitivity to etoposide (VP-16) and increased levels of glutathione. Cancer Res. **57:**5238–5242.
31. **Madon, J., B. Hagenbuch, L. Landmann, P. J. Meier, and B. Stieger.** 2000. Transport function and hepatocellular localization of mrp6 in rat liver. Mol. Pharmacol. **57:**634–641.
32. **Neldner, K. H.** 1988. Pseudoxanthoma elasticum. Clin. Dermatol. **6:**1–159.
33. **Nickoloff, B. J., F. R. Noodleman, and E. A. Abel.** 1985. Perforating pseudoxanthoma elasticum associated with chronic renal failure and hemodialysis. Arch. Dermatol. **121:**1321–1322.
34. **Niizuma, K.** 1983. Pseudoxanthoma elasticum–a fresh approach to morphogenesis using tannic acid fixation. Tokai J. Exp. Clin. Med. **8:**79–88.
35. **Nikko, A. P., M. Dunningan, and C. J. Cockerell.** 1996. Calciphylaxis with histologic changes of pseudoxanthoma elasticum. Am. J. Dermatopathol. **18:**396–399.
36. **Paulusma, C. C., P. J. Bosma, G. J. Zaman, C. T. Bakker, M. Otter, G. L. Scheffer, R. J. Scheper, P. Borst, and R. P. Oude Elferink.** 1996. Congenital jaundice in rats with a mutation in a multidrug resistance-associated protein gene. Science **271:**1126–1128.
37. **Proks, P., F. Reimann, N. Green, F. Gribble, and F. Ashcroft.** 2002. Sulfonylurea stimulation of insulin secretion. Diabetes **51**(Suppl. 3)**:**S368–S376.
38. **Pulkkinen, L., F. Ringpfeil, and J. Uitto.** 2002. Progress in heritable skin diseases: molecular bases and clinical implications. J. Am. Acad. Dermatol. **47:**91–104.
39. **Quinton, P. M.** 1999. Physiological basis of cystic fibrosis: a historical perspective. Physiol. Rev. **79:**S3–S22.
40. **Relyea, M. J., J. Miller, D. Boggess, and J. P. Sundberg.** 2000. Necropsy methods for laboratory mice: biological characterization of a new mutation, p. 57–90. *In* J. P. Sundberg and D. Boggess (ed.), Systematic approach to evaluation of mouse mutations. CRC Press, New York, N.Y.
41. **Ringpfeil, F., A. Nakano, J. Uitto, and L. Pulkkinen.** 2001. Compound heterozygosity for a recurrent 16.5-kb Alu-mediated deletion mutation and single-base-pair substitutions in the *ABCC6* gene results in pseudoxanthoma elasticum. Am. J. Hum. Genet. **68:**642–652.
42. **Ringpfeil, F., L. Pulkkinen, and J. Uitto.** 2001. Molecular genetics of pseudoxanthoma elasticum. Exp. Dermatol. **10:**221–228.
43. **Rychlik, W.** 1993. Selection of primers for polymerase chain reaction, p. 31–40. *In* B. A. White (ed.), PCR protocols: current methods and applications. Humana Press, Totowa, N.J.
44. **Sambrook, J., E. F. Fritsch, and T. Maniatis.** 1989. Molecular cloning: a laboratory manual, 2nd ed. Cold Spring Harbor Laboratory Press, Cold Spring Harbor, N.Y.
45. **Sampath, J., M. Adachi, S. Hatse, L. Naesens, J. Balzarini, R. M. Flatley, L. H. Matherly, and J. D. Schuetz.** 2002. Role of MRP4 and MRP5 in biology and chemotherapy. AAPS Pharm. Sci. **4:**E14.
46. **Sapadin, A. N., M. G. Lebwohl, S. A. Teich, R. G. Phelps, D. DiCostanzo, and S. R. Cohen.** 1998. Periumbilical pseudoxanthoma elasticum associated with chronic renal failure and angioid streaks–apparent regression with hemodialysis. J. Am. Acad. Dermatol. **39:**338–344.
47. **Scheffer, G. L., X. Hu, A. C. Pijnenborg, J. Wijnholds, A. A. Bergen, and R. J. Scheper.** 2002. MRP6 (*ABCC6*) detection in normal human tissues and tumors. Lab. Investig. **82:**515–518.
48. **Secretan, M., L. Zografos, D. Guggisberg, and B. Piguet.** 1998. Chorioretinal vascular abnormalities associated with angioid streaks and pseudoxanthoma elasticum. Arch. Ophthalmol. **116:**1333–1336.
49. **Seghers, V., M. Nakazaki, F. DeMayo, L. Aguilar-Bryan, and J. Bryan.** 2000. *Sur1* knockout mice: a model for K(ATP) channel-independent regulation of insulin secretion. J. Biol. Chem. **275:**9270–9277.
50. **Sheehan, D. C., and B. B. Hrapchak.** 1980. Theory and practice of histotechnology. Mosby, St. Louis, MO.
51. **Shimizu, H., H. Taniguchi, Y. Hippo, Y. Hayashizaki, H. Aburatani, and T. Ishikawa.** 2003. Characterization of the mouse *Abcc12* gene and its transcript encoding an ATP-binding cassette transporter, an orthologue of human ABCC12. Gene **310:**17–28.
52. **Shiota, C., O. Larsson, K. D. Shelton, M. Shiota, A. M. Efanov, M. Hoy, J. Lindner, S. Kooptiwut, L. Juntti-Berggren, J. Gromada, P. O. Berggren, and M. A. Magnuson.** 2002. Sulfonylurea receptor type 1 knock-out mice have intact feeding-stimulated insulin secretion despite marked impairment in their response to glucose. J. Biol. Chem. **277:**37176–37183.
53. **Southern, E. M.** 1975. Detection of specific sequences among DNA fragments separated by gel electrophoresis. J. Mol. Biol. **98:**503–517.
54. **Stewart, C. L.** 1993. Production of chimeras between embryonic stem cells and embryos. Methods Enzymol. **225:**823–855.
55. **Suarez, M. J., J. B. Garcia, M. Orense, E. Raimunde, M. V. Lopez, and O. Fernandez.** 1991. Sonographic aspects of pseudoxanthoma elasticum. Pediatr. Radiol. **21:**538–539.
56. **Sundberg, J. P., and L. E. King.** 2000. Skin and its appendages: normal anatomy and pathology of spontaneous, transgenic, and targeted mouse mutations, p. 181–213. *In* J. Ward, J. F. Mahler, R. R. Maronpot, and J. P. Sundberg (ed.), Pathology of genetically engineered mice. Iowa State University Press, Ames, Iowa.
57. **Sundberg, J. P., and L. E. King, Jr.** 1996. Mouse mutations as animal models and biomedical tools for dermatological research. J. Investig. Dermatol. **106:**368–376.
58. **Tammur, J., C. Prades, I. Arnould, A. Rzhetsky, A. Hutchinson, M. Adachi, J. D. Schuetz, K. J. Swoboda, L. J. Ptacek, M. Rosier, M. Dean, and R. Allikmets.** 2001. Two new genes from the human ATP-binding cassette transporter superfamily, ABCC11 and *ABCC12*, tandemly duplicated on chromosome 16q12. Gene **273:**89–96.
59. **Trip, M. D., Y. M. Smulders, J. J. Wegman, X. Hu, J. M. Boer, J. B. ten Brink, A. H. Zwinderman, J. J. Kastelein, E. J. Feskens, and A. A. Bergen.** 2002. Frequent mutation in the *ABCC6* gene (R1141X) is associated with a strong increase in the prevalence of coronary artery disease. Circulation **106:**773–775.

60. **Tybulewicz, V. L., C. E. Crawford, P. K. Jackson, R. T. Bronson, and R. C. Mulligan.** 1991. Neonatal lethality and lymphopenia in mice with a homozygous disruption of the *c-abl* proto-oncogene. Cell **65:**1153–1163.
61. **Uitto, J., and L. Pulkkinen.** 2002. Heritable diseases affecting the elastic tissues: cutis laxa, pseudoxanthoma elasticum, and related disorders, p. 4044–4068. *In* D. L. Rimoin, J. M. Connor, R. Pyeritz and B. R. Korf (ed.), Emery and Rimoin's principles and practice of medical genetics. Churchill Livingstone, New York, N.Y.
62. **Uitto, J., L. Pulkkinen, and F. Ringpfeil.** 2001. Molecular genetics of pseudoxanthoma elasticum: a metabolic disorder at the environment-genome interface? Trends Mol. Med. **7:**13–17.
63. **Wijnholds, J., R. Evers, M. R. van Leusden, C. A. Mol, G. J. Zaman, U. Mayer, J. H. Beijnen, M. van der Valk, P. Krimpenfort, and P. Borst.** 1997. Increased sensitivity to anticancer drugs and decreased inflammatory response in mice lacking the multidrug resistance-associated protein. Nat. Med. **3:**1275–1279.
64. **Yabuuchi, H., S. Takayanagi, K. Yoshinaga, N. Taniguchi, H. Aburatani, and T. Ishikawa.** 2002. *ABCC13*, an unusual truncated ABC transporter, is highly expressed in fetal human liver. Biochem. Biophys. Res. Commun. **299:**410–417.
65. **Yap, E. Y., M. S. Gleaton, and H. Buettner.** 1992. Visual loss associated with pseudoxanthoma elasticum. Retina **12:**315–319.